

Intermittency and correlations in 200 GeV/nucleon S+S and S+Au collisions

R. Albrecht,¹ A. Antonenko,² T. C. Awes,³ F. Berger,⁴ M. A. Bloomer,⁵ D. Bock,⁴ R. Bock,¹ G. Claesson,⁶ G. Clewing,⁴ L. Dragon,⁴ A. Eklund,⁶ S. Fokin,² A. Franz,^{3,*} S. Garpman,⁶ R. Glasow,⁴ H. Å. Gustafsson,⁶ H. H. Gutbrod,¹ M. Hartig,⁴ X. He,⁷ G. Hölker,⁴ J. Idh,⁶ M. Ippolitov,² P. Jacobs,⁵ K. H. Kampert,⁴ K. Karadjev,² B. W. Kolb,¹ A. Lebedev,² H. Löhner,⁸ I. Lund,^{1,8} V. Manko,² S. Nikolaev,² J. Nystrand,⁶ F. E. Obenshain,³ A. Oskarsson,⁶ I. Otterlund,⁶ T. Peitzmann,⁴ F. Plasil,³ A. M. Poskanzer,⁵ M. Purschke,^{4,1} H.-G. Ritter,⁵ B. Roters,^{4,1} S. Saini,³ R. Santo,⁴ H. R. Schmidt,¹ K. Söderström,⁶ S. P. Sørensen,^{3,7} K. Steffens,⁴ P. Steinhäuser,^{4,1} E. Stenlund,⁶ D. Stüken,⁴ A. Vinogradov,² and G. R. Young³

¹*Gesellschaft für Schwerionenforschung, D-64220 Darmstadt, Germany*

²*Kurchatov Institute, Kurchatov Square, 123182 Moscow, Russia*

³*Oak Ridge National Laboratory, Oak Ridge, Tennessee 37831*

⁴*University of Münster, D-48149 Münster, Germany*

⁵*Lawrence Berkeley Laboratory, Berkeley, California 94720*

⁶*University of Lund, S-22362 Lund, Sweden*

⁷*University of Tennessee, Knoxville, Tennessee 37996*

⁸*Kernfysisch Versneller Instituut, University of Groningen, NL-9747 AA Groningen, Netherlands*

(Received 14 February 1994)

We have studied one- and two-dimensional scaled factorial moments in $^{32}\text{S}+\text{S}$ and $^{32}\text{S}+\text{Au}$ collisions at 200 GeV/nucleon in a high statistics electronic measurement at the CERN SPS using pad-readout streamer tubes. We observe no intermittency signal beyond that produced by folding the FRITIOF event generator with a detailed model of our detector. The systematic effects of detector response, two-track separation, and finite statistics in a factorial moment analysis are discussed in detail. Even though the observed signal contains measurable distortions due to these experimental effects, we show that we are sensitive to intermittency. As an alternative method, a two-particle correlation function analysis was applied to the same data to measure correlated particle production at small scales. We show that this method does not suffer as much as the factorial moment analysis does from distortions due to the limited two-track resolution of the detector. The correlation functions also agree with the predictions of FRITIOF filtered through our detector simulation, down to the limit of the two-track resolution. Since FRITIOF models nucleus-nucleus collisions by the superposition of nucleon-nucleon collisions, we conclude that there is no evidence in our data of the kinds of collective behavior predicted to give strong intermittency in heavy ion collisions.

PACS number(s): 25.75.+r, 24.60.Ky

I. INTRODUCTION

The phase-space distribution of hadrons produced in high-energy collisions has been used for many years as a tool to investigate the elementary mechanisms governing such reactions. Models incorporating perturbative QCD for hard (i.e., high-momentum transfer) scattering and semiphenomenological formulations for soft (low-momentum transfer) collisions and hadronization have met with great success in describing *single-particle* distributions in systems as simple as e^+e^- (e.g., JETSET [1] and HERWIG [2]) and as complex as nucleus-nucleus collisions (e.g., RQMD [3], VENUS [4], and FRITIOF [5]). In addition, *large phase-space scale multiparticle* distributions in collisions dominated by hard processes (i.e., jets) are also well described by such models. In recent years, interest has grown in the investigation of *small phase-space scale* multiparticle distributions [6]. The ini-

tial impetus for this came from the study of high-energy nucleus-nucleus collisions [7,8], in connection with a possible phase transition from ordinary hadronic matter to a quark-gluon plasma. However, it was soon realized that such a detailed study of multiparticle distributions in simpler collisions may also yield new information on elementary particle production mechanisms, possibly relating to their fractal properties [9]. Thus, there are two quite separate goals for the current study of multiparticle production: (i) the investigation of elementary particle production mechanisms, using simple probes, and (ii) the search for collective phenomena, usually using complex probes such as heavy nuclei. The strategy to identify collective phenomena is to search for deviations from the multiparticle distributions predicted by a simple superposition of elementary sources.

Measurements of multiparticle distributions require great care to interpret because of the unavoidable fluctuations due to finite particle multiplicity, resonance production, and detector effects such as interactions with material and limited two-track resolution. Białas and Peschanski [7,8] suggested a means of suppressing the fluctuations due to finite multiplicity by calculating the

*Now at CERN, CH-1211 Geneva 23, Switzerland.

mean scaled factorial moments $\langle F_q \rangle$ of the multiplicity distribution. Given a total interval of (e.g., rapidity) Δy divided into M equal bins of size $\delta y = \Delta y/M$, the mean scaled factorial moment $\langle F_q \rangle$ of order q is defined as

$$\langle F_q \rangle = \frac{1}{M} \frac{\sum_{m=1}^M \langle n_m(n_m-1) \cdots (n_m-q+1) \rangle}{\langle n \rangle^q}, \quad (1)$$

where n_m denotes the population of bin m , $\langle \cdots \rangle$ indicates an average over events, and $\langle n \rangle$ is the mean multiplicity within δy [10]. The dynamics of the particle production mechanism are then reflected in the dependence of $\langle F_q \rangle$ on δy . In particular, a mechanism with a self-similar (“branching”) structure would exhibit a power-law dependence:

$$\langle F_q \rangle \propto \delta y^{-\phi_q}. \quad (2)$$

This power-law dependence is known as *intermittency*, and the general study of the dependence of $\langle F_q \rangle$ on δy has come to be known by that name. The slope in a plot of $\ln(\langle F_q \rangle)$ vs $-\ln \delta y$ is ϕ_q .

Bialas and Peschanski [7] proposed that particle production in a longitudinally expanding fluid of quark-gluon plasma has an underlying branching structure in rapidity, leading to clustering in rapidity of final-state hadrons (i.e., intermittency in the multiplicity distribution). Others have suggested that the occurrence of intermittency is a signal of a second-order phase transition [11]. However, more elementary particle production mechanisms having a self-similar cascading structure, such as the fragmentation of strings (e.g., [12] and references therein) or high-energy jets [13], are also expected to produce intermittent final-state distributions. Whatever the underlying physics, the analysis of scaled factorial moments has served as a sensitive statistical tool to compare particle production models to data. The hope is that, after accounting for all experimental effects, differences between models and data will point to new physics.

There have been extensive experimental investigations of intermittency in the last few years. For the case of e^+e^- collisions, almost all studies find agreement in detail between data and commonly used particle production models [14,15] (but see also [16]). The situation with hadronic probes is much less clear. In particular, the question of intermittency in high-energy nucleus-nucleus collisions is unsettled. The KLM [17] collaboration has reported slopes that cannot be accounted for by common particle production models, and which increase with increasing dimensionality of the partitioning of phase space. On the other hand, the Helios-Emulsion Collaboration [18] reports no slopes beyond those accounted for by folding common particle production models with a model of experimental effects. The EMU01 Collaboration [19,20] observes a somewhat larger effect than obtained by FRITIOF plus gamma conversion. There are, however, no Bose-Einstein correlations present in their FRITIOF version, and they argue that this might account for the difference. The NA35 [21] collaboration observes a strong effect which they claim can be explained once

Bose-Einstein correlations are incorporated into FRITIOF.

All of the reported heavy-ion results are from visual experiments, with their attendant low statistics. This paper reports on results from the electronic heavy-ion experiment WA80, which measured heavy-ion collisions of $^{32}\text{S}+\text{S}$ and $^{32}\text{S}+\text{Au}$ at 200 GeV/nucleon at the CERN SPS. Electronic experiments have the advantages over visual detectors of a more selective central trigger with much higher statistics. However, they suffer from reduced spatial resolution, leading to a more limited two-track separation, reduced ability to distinguish backgrounds such as γ conversions and hadronic showering in matter, and smaller acceptance. We have made a careful study of track reconstruction and background effects, and present both one- and two-dimensional [13] scaled factorial moment analyses of $^{32}\text{S}+\text{S}$ and $^{32}\text{S}+\text{Au}$ collisions at 200 GeV/nucleon. In addition, we have performed a two-particle correlation function analysis on the same set of data. This minimizes our sensitivity to these detector artefacts while remaining sensitive to correlated particle production.

WA80 has previously reported the observation of significant intermittency in ^{16}O -induced reactions at 200 GeV/nucleon [22]; however, because of an error in the track reconstruction those results are incorrect for close-track correlations. This paper presents a new analysis, based on a reconfigured and calibrated detector and a completely new analysis procedure.

In Sec. II of this paper we describe the WA80 experimental setup, running conditions at which data were taken, and the criteria by which central events are distinguished from peripheral ones. In Sec. III, the Streamer Tube Arrays and the method by which individual charged particle tracks were reconstructed and measured are described. Details on the factorial moment analysis are in Sec. IV. The detector simulation based on GEANT is described in Sec. V. Results of the factorial moment analysis are presented in Sec. VI, including detailed comparisons to FRITIOF filtered through the detector simulation. Our sensitivity to intermittency is investigated in Sec. VII using an alpha model calculation. Some experimental biases that we observed but which affect nearly all factorial moment analyses are discussed in Sec. VIII. The scaling of factorial moments is investigated in Sec. IX. In Sec. X, we show the results of a two-particle correlation function analysis and in Sec. XI discuss its relevance to the search for intermittency for real detectors. We draw our conclusions in Sec. XII.

II. EXPERIMENTAL SETUP

The 1990 setup for the WA80 experiment [23] is shown in Fig. 1. This setup is considerably different from the initial configuration of WA80 [24] for the following reasons: the lead glass array SAPHIR [25] was reconfigured; the midrapidity calorimeter (MIRAC) and the zero-degree calorimeter (ZDC) [26] were moved further downstream, now subtending the pseudorapidity intervals of $3.0 < \eta < 5.9$ and $6.5 < \eta$, respectively; the Plastic Ball was removed; and most importantly for this analy-

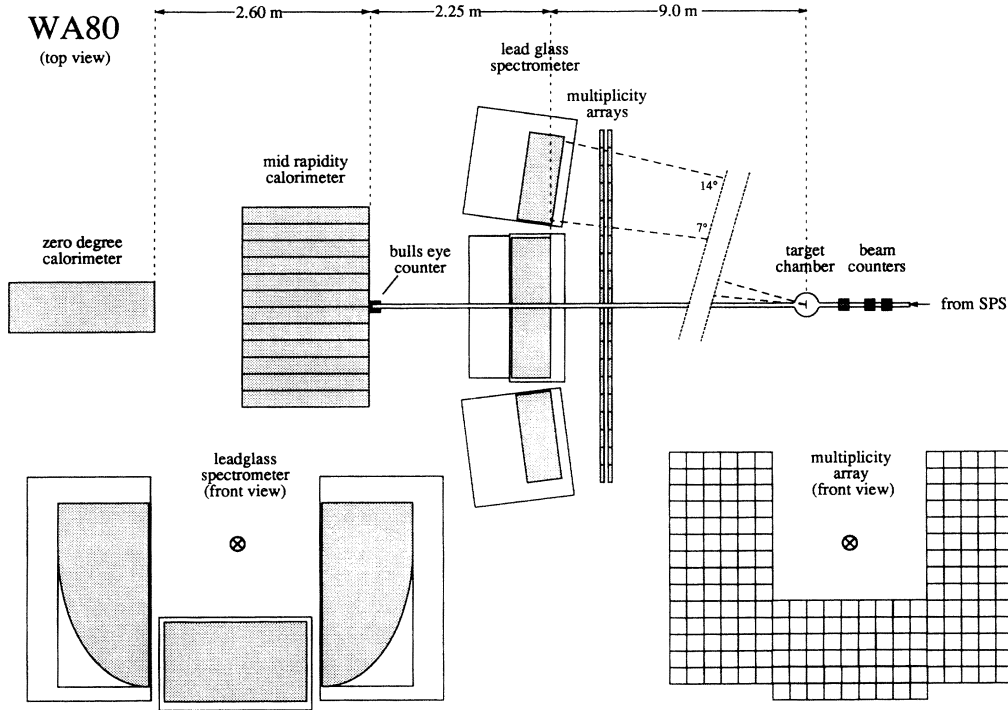


FIG. 1. 1990 WA80 experimental setup.

sis, the large-area, high-granularity streamer tube arrays [27] were reconfigured in order to serve as a charged particle veto for the lead glass spectrometer, as well as to measure multiplicity distributions.

For the present analysis, the streamer tube array measured the pseudorapidity η and azimuthal angle ϕ of charged particles within an interval of $2 < \eta < 3$ and $\approx 60\%$ of 2π in ϕ . The pseudorapidity and multiplicity distributions have been previously published [28]. MIRAC and ZDC provided transverse energy E_T and forward energy E_F , respectively, and were used in this study exclusively for event selection. The lead glass spectrometer was not used in this analysis.

Data were taken with a ^{32}S beam of 200 GeV/nucleon, incident on S (205 mg/cm²) and Au (250 mg/cm²) targets. The minimum bias trigger condition (also different from previous WA80 runs) was defined by the following two requirements: (a) $E_T > E_T^{\text{thresh}}$ measured in MIRAC, where E_T^{thresh} was about one GeV, and (b) Z_{proj} , measured by a Cherenkov bull's eye counter in front of the ZDC, was less than 15 charge units.

Peripheral and central events were selected in the analysis by software cuts on the energies observed in MIRAC

($3.0 < \eta < 5.9$) and ZDC ($\eta > 6.5$) for a sample of events taken with a minimum bias hardware trigger. The energy sums used were corrected for leakage and gain variations of the photomultiplier tubes. Nontarget events dominate the population having low values of E_T . These events are removed by incorporating a cut $E_T > E_T^{\text{min}}$ in the definition of the peripheral trigger. The definition of the peripheral and central software triggers is as follows:

$$\text{peripheral} = \text{min bias} \cap (E_T > E_T^{\text{min}}) \cap (E_F > E_F^{\text{high}}),$$

$$\text{central} = \text{min bias} \cap (E_T > E_T^{\text{high}}).$$

Effectively the ZCD is used to define peripheral events, and MIRAC is used to define central events. The actual energy values used in software to define these triggers are shown in Table I. Using these triggers, the total number of events used in the analysis are also shown, along with the corresponding fraction of the total cross section each trigger represents.

TABLE I. Trigger cuts, number of events and fraction of total measured cross section.

Target	E_T^{min} (GeV)	E_F^{high} (GeV)	E_T^{high} (GeV)	Peripheral		Central	
				No. events	Fraction	No. events	Fraction
S	10.0	5 800	56.5	227 560	0.21	323 220	0.14
Au	10.0	5 500	90.0	213 560	0.19	270 420	0.20

III. STREAMER TUBE ARRAYS

The streamer tubes were of the Larrocci type [29]. They were arranged in two planes perpendicular to the beam, with each layer covered with 2×10^4 capacitively coupled pads with pad sizes varying according to the radial distance from the beam. The pads were connected to discriminators so that a yes/no signal was generated, depending on the passage of a charged particle through the gas volume behind a pad. The pads were arranged in groups of 24, 40, or 160 on printed circuit boards of size $21 \times 21 \text{ cm}^2$. The region of the streamer tube arrays used in the analysis (see Fig. 4) was predominantly occupied by the 160-pad boards, having pad dimensions of 1.05 cm by 2.625 cm along x and y , respectively. Each board had a single threshold setting for all its pads.

One or more pads would “fire” (i.e., exceed the threshold voltage) in response to a streamer that develops after the passage of a charged particle. The response of pads to individual charged particles was measured in calibration runs, using a beam of 10 GeV e^- and π^- . It was found that the passage of a single charged particle will induce a signal on a cluster of contiguous pads. Less than 1% of the single charged particles will induce two or more disconnected clusters. It was also found that the “geometric” centroid of clusters (weighted by the area of the fired pads) determines the position at which a charged particle passed through the streamer tubes for all cluster patterns, within an accuracy of $\approx \pm 4 \text{ mm}$ horizontally and $\pm 6 \text{ mm}$ vertically (due to the larger length of the pad vertically than horizontally). Single track efficiencies varied between 85 and 95% among readout boards, where the inefficiency is due to tracks which traverse the streamer tube walls instead of the gas volume. For a given location on the detector there is a distribution of sizes and shapes of the single-particle clusters, and this distribution can vary over the face of the detector depending upon the local threshold setting and the mechanical coupling of the pads to the streamer tubes. About ten different cluster patterns, those with the fewest number of fired pads, accounted for 90% of all single-hit clusters. The patterns of the ten most probable clusters as measured in the calibration data are drawn in Fig. 2.

A new analysis chain to extract tracks from pad hits was developed for the scaled factorial moment analysis. Particular attention was paid to optimize the resolution in order to distinguish two tracks and to reject tracks that did not originate from the target. The analysis chain consisted of the following elements.

(1) Clustering: For each plane separately, clusters (groups of connected “fired” pads) were formed.

(2) Correlating clusters: Clusters on both planes were projected onto a common plane along a line that joined

the cluster centroid with the target. Correlated clusters were those for which fired pads of a cluster on one detector plane overlapped those of the other. These correlated clusters were used as candidates for track reconstruction. Uncorrelated clusters were not considered any further.

(3) Resolving pairs into tracks: All pairs of correlated clusters were resolved into tracks, where each cluster contributed to no more than one track (i.e., clusters could not be shared by tracks). One exception to this rule was allowed, in order to extend the two-track resolution: the situation where exactly two disconnected clusters on one plane correlated with the same cluster on the other plane.

For a typical minimum bias $^{32}\text{S}+\text{Au}$ event, roughly 59.6% of all clusters on a plane formed tracks, 39.6% were uncorrelated with any other cluster, and the remaining 0.8% shared a cluster on the opposite plane with two or more nearby clusters on the same plane, and thus were not used to form tracks. These percentages varied slightly depending on the centrality of the collision. Uncorrelated clusters were due to (i) the finite efficiency of the streamer tubes, and (ii) background clusters due to large-angle particles created from the showering of high pseudorapidity reaction products in the beam pipe. In the latter case, even though these particles could generate clusters on both planes of the streamer tubes, these clusters would not be correlated during reconstruction because of the demand that tracks used in the analysis originate from the target. In order to reduce the rate of false tracks from the random alignment of these “background” clusters, it was essential to determine the optimal cluster size to be used when correlating clusters. Using a Monte Carlo simulation of the WA80 streamer tube detector (described in Sec. V below), we tested our reconstruction efficiency by varying a parameter which increased or decreased the effective size of clusters. It was found that the actual geometrical size of clusters worked best for maximizing the ratio of accurately reconstructed tracks to false tracks.

The relative alignment of the streamer tube planes was determined using tracks from central $^{32}\text{S}+\text{Au}$ events in which the clusters in both planes were single-pad clusters. This procedure determined the relative positions of the planes to within $\pm 2 \text{ mm}$. The absolute position of the plane nearest to the target was determined by surveying to $\pm 4 \text{ mm}$ in both x and y . Altogether we obtain a single-track resolution of $\sigma_\eta \approx \pm 0.002(\text{stat}) \pm 0.003(\text{syst})$ and $\sigma_\phi \approx \pm 0.003(\text{stat}) \pm 0.003(\text{syst})$. The statistical error refers to the measurement uncertainty, while the systematic error refers to the errors in relative alignment and absolute position determination.

The two-track resolution has been determined in two independent ways. One method uses the data itself in a two-particle correlation analysis (described in Sec. X be-



FIG. 2. Patterns of the ten most probable clusters as observed in the calibration data.

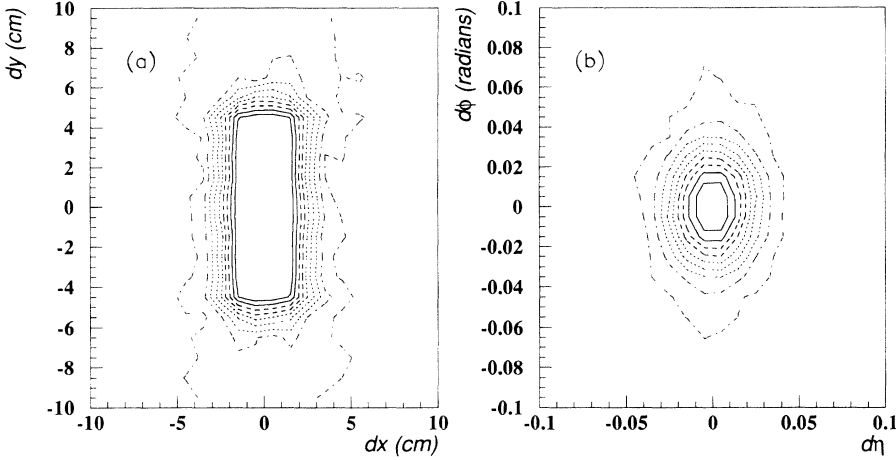


FIG. 3. Two-particle correlation distributions in (a) $dx - dy$ and (b) $d\eta - d\phi$ space for central $^{32}\text{S}+\text{Au}$ collisions. The linear contours represent the “hole” due to the finite two-track resolution of the streamer tube detector. The distributions have a value of ≈ 1 far from the hole and drop to zero within it. The cell size is 1 cm by 1 cm in (a) and 0.01 by 0.01 in (b).

low), which works when the observed correlations are not too strong. Figure 3 is a contour plot of the two-particle correlation functions in $dx - dy$ and $d\eta - d\phi$ space for central $^{32}\text{S}+\text{Au}$ collisions, where $dx = x_1 - x_2$ and x_1 and x_2 are the x positions for a pair of tracks on a streamer tube plane 784.7 cm from the target (similarly for dy , $d\eta$, and $d\phi$). As dx and dy become smaller, the correlation function falls rapidly from ≈ 1 to zero, reflecting a reduced efficiency for resolving close pairs. The two-track resolution is limited by the size of individual clusters: for pairs of tracks below a certain separation, the clusters each track produces merge into a single large cluster and can no longer be distinguished. The two-particle acceptance “hole” in $dx - dy$ corresponds to the observed hole in $d\eta - d\phi$ space. From inspection of Fig. 3 we obtain the following two-track resolutions, measured as the half-width at half-maximum along the respective axes:

$$dx : 2.4 \text{ cm}, \quad d\eta : 0.022 ,$$

$$dy : 5.4 \text{ cm}, \quad d\phi : 0.027 .$$

The two-track resolution is about a factor of 10 larger than the single-track resolution, though it is still relatively small compared to other experiments. Even so, it constitutes the single most important experimental effect on the behavior of factorial moments at high resolution in our analysis.

The second method for estimating the two-track reso-

lution uses the measured cluster sizes and probabilities as obtained from the calibration data of the 160-pad boards. In this case the two-track resolution in the x or y direction is equal to the average cluster size in that direction plus the width of one pad, where a pad has dimension 1.05 cm in x and 2.625 cm in y . This criterion constitutes the minimum distance that must obtain between two distinguishable clusters. Using this criterion, the measured two-track resolutions are $dx = 2.4$ cm and $dy = 6.2$ cm, in qualitative agreement with the values obtained using the first method.

IV. DATA ANALYSIS

A factorial moment analysis was performed using tracks within the pseudorapidity interval $2.12 \leq \eta \leq 2.57$ ($\Delta\eta = 0.45$) and azimuthal angle interval $-110^\circ \leq \phi \leq 110^\circ$ ($\Delta\phi = 220^\circ$). This region on the front plane of the streamer tube array for these phase-space intervals is shown in Fig. 4. The uppermost part of the detector is not used because it is populated by boards with large pads.

In order to avoid introducing biases in the estimation of the factorial moments, it is necessary to have uniform acceptance within $\Delta\eta$ and $\Delta\phi$. This dictated the choice of a rather restricted phase-space interval compared to other intermittency analyses. Bin multiplicities were calculated for the following subdivisions of these intervals:

$$\delta\eta = \Delta\eta/m, \quad m = 1, \dots, 8 \text{ (one-dimensional analysis in } \eta \text{)}, \quad (3)$$

$$(\delta\eta = \Delta\eta/m) \simeq (\delta\phi = \Delta\phi/8m), \quad m = 1, \dots, 6 \text{ (two-dimensional analysis in } \eta - \phi \text{)}, \quad (4)$$

which were then summed to obtain the scaled factorial moments $\langle F_q \rangle$ as follows:

$$\langle F_q \rangle = \frac{1}{N_{\text{events}}} \sum_{i=1}^{N_{\text{events}}} M^{q-1} \frac{\sum_{m=1}^M n_{m,i}(n_{m,i}-1) \cdots (n_{m,i}-q+1)}{\langle N \rangle^q}, \quad (5)$$

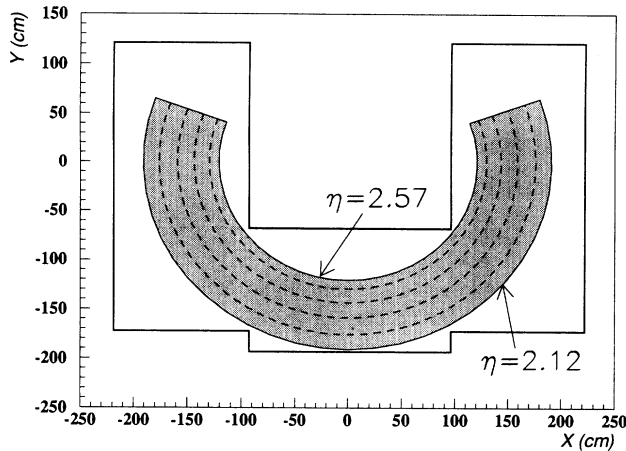


FIG. 4. Phase-space acceptance for scaled factorial moment analysis ($\Delta\eta = 0.45$, $\Delta\phi = 220^\circ$). Solid line indicates outline of actual streamer tube detector.

where N_{events} is the total number of events analyzed, M is the total number of bins in η and ϕ , m is the bin index, $n_{m,i}$ is the number of particles in bin m for event i , and $\langle N \rangle^q$ is the average multiplicity within $\Delta\eta - \Delta\phi$. This analysis is called “horizontal” because the scaled factorial moments are calculated by first summing over bins and then averaging over events [19]. At least five events were required to contribute to a moment in order to calculate it at a given resolution [15]. No correction for the variation of $dN/d\eta$ [30] was necessary due to our

narrow pseudorapidity acceptance.

Factorial moments in both the one-dimensional and two-dimensional analyses were estimated by dividing the data into subsamples of 2000 events each and calculating $\langle F_q \rangle$ for each subsample. For large enough phase-space bins, the resulting $\langle F_q \rangle$ subsample distributions were sufficiently Gaussian that the mean value and the variance of the distributions can be used as estimates of $\langle F_q \rangle$ and the statistical errors of $\langle F_q \rangle$, respectively. This method is similar to one developed independently and reported in Ref. [31]. Typical distributions of $\langle F_q \rangle$ from subsamples are shown in Fig. 5 for a two-dimensional analysis of $^{32}\text{S}+\text{Au}$ collisions. A general feature of these distributions is that the $\langle F_q \rangle$ distributions become more asymmetric and broader for a fixed number of subsample events as the bin multiplicity becomes smaller (i.e., as phase space is subdivided into smaller bins). This effect is more dramatic for the higher order moments, as has been studied in detail in Ref. [31]. For some moments, such as $\langle F_5 \rangle$ in Figs. 5(b) and (d), the distributions can be highly non-Gaussian and noticeably discrete. We restrict the data presented later in this article to those moments whose distributions are symmetric and well behaved.

V. SIMULATIONS

Experimental effects can generate artificial correlations or suppress the correlations that are present in the true phase-space distribution of particles from the collision. In order to assess these experimental effects, we have

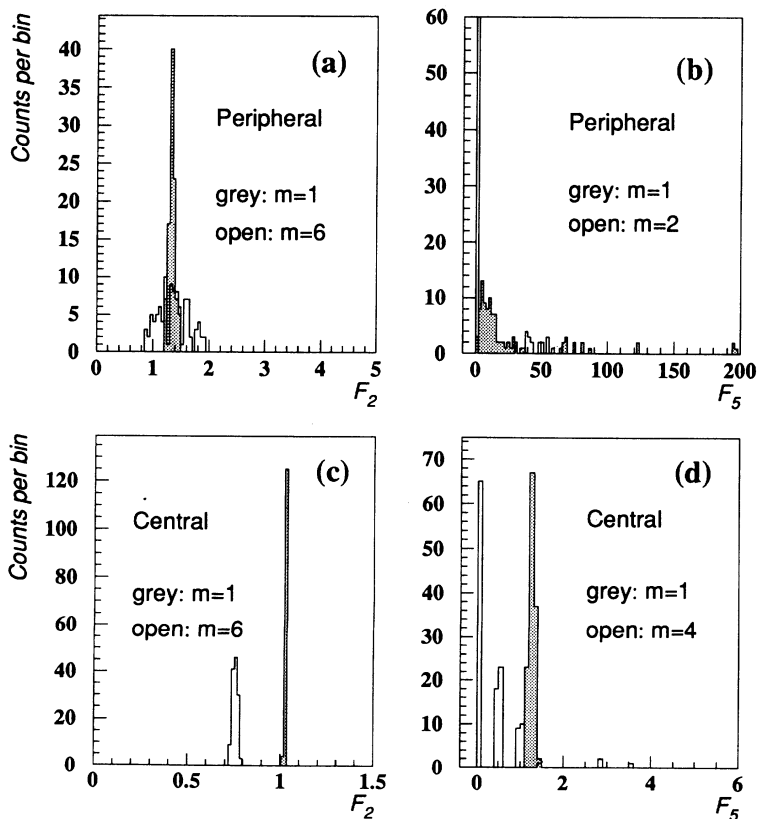


FIG. 5. Subsample distributions of $\langle F_q \rangle$ for a two-dimensional analysis of $^{32}\text{S}+\text{Au}$ collisions. Each frame shows the distributions of the same moment for different bin sizes. Peripheral events: (a) $\langle F_2 \rangle$ and (b) $\langle F_5 \rangle$. Central events: (c) $\langle F_2 \rangle$ and (d) $\langle F_5 \rangle$.

performed detailed simulations of the WA80 setup using the detector modeling program GEANT v3.15 [32] fed by events from the FRITIOF event generator v1.7 [5]. This version of FRITIOF does not include Bose-Einstein correlations, unlike what was done by NA35 [21]. In addition to modeling the generation or suppression of tracks due to interactions in matter, we have developed a model of the response of the streamer tube detector. As described above, the detector readout is segmented into readout boards. Due to electronic and mechanical variations among the boards, the local response of the detector (in particular, the frequency of certain cluster patterns and the overall efficiency of the readout board) can vary. The detector also had an inefficiency due to the dead area occupied by the streamer tube walls. The response of each readout board for each plane was determined from low multiplicity $^{32}\text{S}+\text{S}$ events in the actual physics runs, and was characterized by the distribution of sizes and shapes of clusters observed in that region. It was assumed that the overall efficiency of each readout board was 90%. We did not attempt to model single-charged tracks yielding two disconnected clusters, as observed in the calibration data, because the probability that a track produce two distinct clusters on both planes is negligible for this analysis. This local response was then used in the simulation for the same region of the detector, pad hits were generated according to the cluster distribution, and the simulated events were passed through the same analysis chain that was used to process the raw data.

An approximate model of the WA80 trigger was developed, based on the geometrical acceptance of MIRAC

and ZDC, to select central or peripheral events in the simulation in the same way as in data analysis.

VI. RESULTS

Multiplicity distributions within the acceptance of the scaled factorial moment analysis for central and peripheral collisions are shown for both data and simulations in Fig. 6. The results presented as Monte Carlo in the following plots refer to the entire detector simulation as described in the previous section. With the exception of central $^{32}\text{S}+\text{Au}$, good agreement is obtained for all distributions, showing that the Monte Carlo reproduces well the gross features of these multiplicity distributions, though the distributions for the data are slightly broader than those for the simulation. The disagreement seen for $^{32}\text{S}+\text{Au}$ collisions might be a consequence of low momentum protons from the fragmentation of the Au target nucleus [28], which are not included in the FRITIOF event generator. The disagreement may also reflect the enhanced fluctuations in total multiplicity expected in heavy-ion collisions due to cross section fluctuations [33]. Table II lists the mean multiplicity $\langle n \rangle$ and rms for the distributions shown in Fig. 6. The small ($\sim 10\%$) disagreement for central $^{32}\text{S}+\text{Au}$ does not effect our study, as will be shown below.

Figure 7 shows factorial moments $\ln\langle F_2 \rangle$ through $\ln\langle F_5 \rangle$ from a one-dimensional analysis [Eq. (5)] for peripheral and central $^{32}\text{S}+\text{S}$ and $^{32}\text{S}+\text{Au}$ collisions. The factorial moments of all orders do not increase signif-

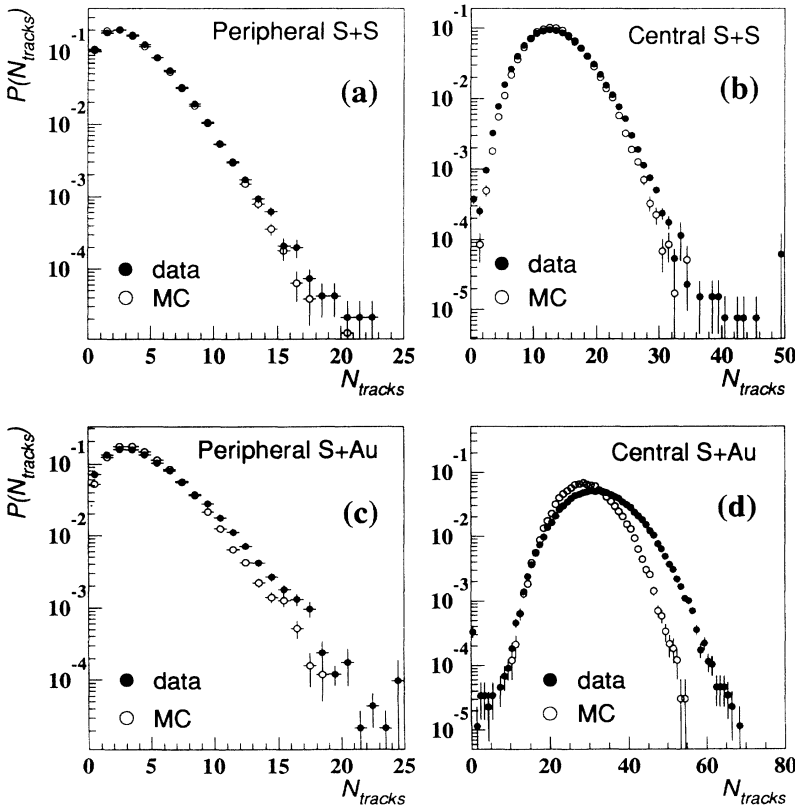


FIG. 6. Probability distribution to obtain N tracks in the WA80 acceptance for (a) peripheral and (b) central $^{32}\text{S}+\text{S}$ collisions, as well as (c) peripheral and (d) central $^{32}\text{S}+\text{Au}$ collisions. Solid points, data; open points, Monte Carlo.

TABLE II. Mean multiplicity and rms within acceptance of the analysis for all triggers used. Values in parentheses are for the Monte Carlo.

Reaction	$\langle n \rangle$	rms
Peripheral $^{32}\text{S}+\text{S}$	3.06 (2.90)	2.34 (2.22)
Central $^{32}\text{S}+\text{S}$	13.2 (12.9)	4.37 (3.98)
Peripheral $^{32}\text{S}+\text{Au}$	3.97 (3.82)	2.98 (2.54)
Central $^{32}\text{S}+\text{Au}$	31.7 (29.7)	7.67 (6.09)

icantly as $\delta\eta$ decreases, as would be expected if one-dimensional intermittency were present. In fact, the moments from central $^{32}\text{S}+\text{Au}$ collisions *decrease* at higher resolution. This “sagging” of the moments is a detector artifact due primarily to the two-track resolution of the streamer tube array and the high multiplicity densities encountered in central collisions, as will be shown in the next section.

We now present detailed comparisons of $\langle F_2 \rangle$ between data and our simulations in order to address the question of intermittency. Factorial moments $\ln\langle F_2 \rangle$ for both data (solid circles) and simulations (open circles) are shown in Figs. 8 and 9 for one-dimensional (η) and two-dimensional ($\eta - \phi$) scaled factorial moment analyses, respectively. In these and all following plots, the $\langle F_2 \rangle$ of all Monte Carlo results on a plot have been scaled so that their leftmost points have the same value as the leftmost data point. This permits the expansion of the vertical scale to show the differences in slopes between

distributions. We choose this means of display of the data to emphasize the physically important parameter of the data (the slope ϕ_q) while suppressing the modest difference in the magnitude of $\langle F_2 \rangle$ between the Monte Carlo and the data. The difference in magnitude of the moments may be due to inaccuracies in the predictions of resonance production by the model. We cannot address this issue with the present set of data, and argue that unusual reaction dynamics will be reflected solely in the slope ϕ_q . For reference the factors used to scale the Monte Carlo moments are listed in the captions of Figs. 8 and 9.

Concentrating first on Fig. 8, we see that the moments from peripheral collisions show some increase with decreasing $\delta\eta$. The significant sagging of the moments from central collisions makes the determination of any slope impossible (however, note the extremely expanded vertical scale in these plots). In all cases, the trends of the data are well matched by that of the Monte Carlo, which contradicts the observation of one-dimensional intermittency as reported by the EMU01 [19,20] collaboration.

These trends are amplified in Fig. 9 for the moments of the two-dimensional analysis. Peripheral collisions show a much stronger intermittency signal than was observed in the one-dimensional analysis. Sagging dominates even more the behavior of the moments at high resolution for central collisions. The Monte Carlo, which incorporates the two-track resolution of the streamer tube array, is able to reproduce all of these trends for $^{32}\text{S}+\text{S}$ collisions. For $^{32}\text{S}+\text{Au}$ collisions, however, the moments of the data

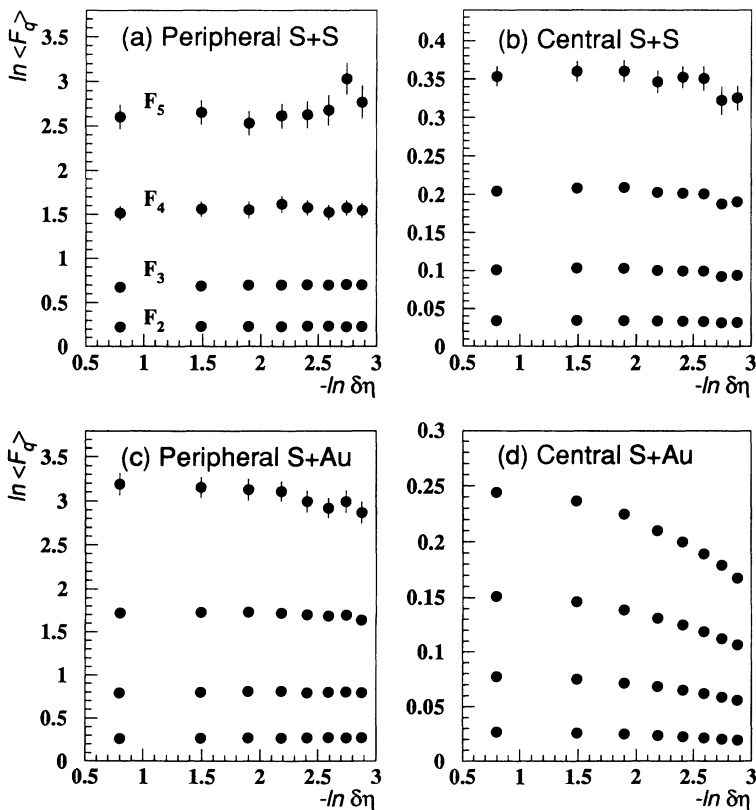


FIG. 7. $\ln\langle F_2 \rangle$ through $\ln\langle F_5 \rangle$ vs $-\ln(\delta\eta)$ for (a) peripheral $^{32}\text{S}+\text{S}$, (b) central $^{32}\text{S}+\text{S}$, (c) peripheral $^{32}\text{S}+\text{Au}$, and (d) central $^{32}\text{S}+\text{Au}$ collisions.

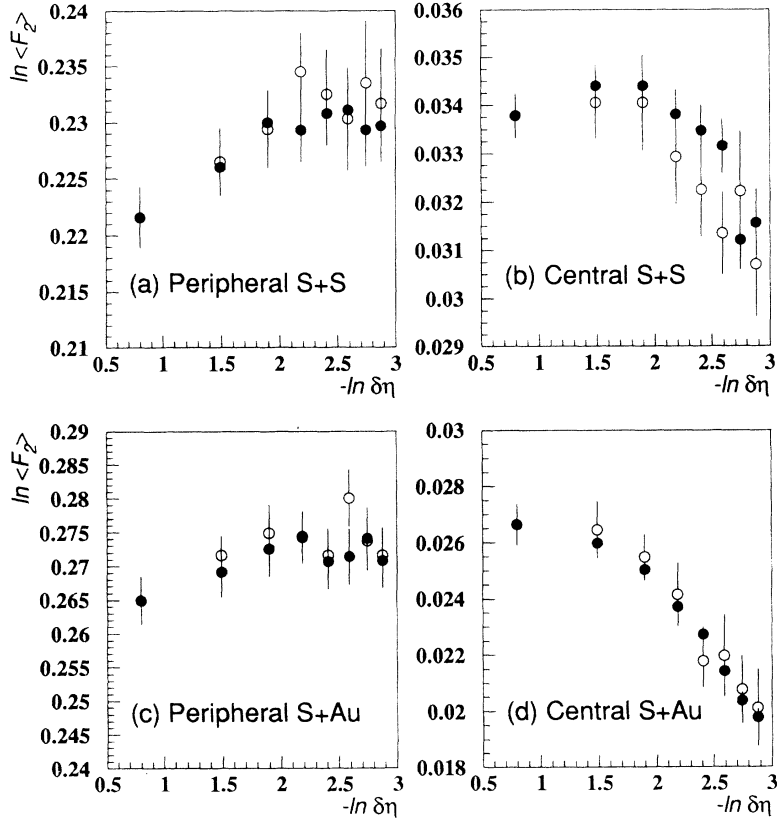


FIG. 8. $\ln\langle F_2 \rangle$ as a function of $-\ln(\delta\eta)$, for (a) peripheral and (b) central $^{32}\text{S}+\text{S}$ collisions, (c) peripheral and (d) central $^{32}\text{S}+\text{Au}$ collisions. Solid points, data; open points, Monte Carlo. The moments of the Monte Carlo calculation have been scaled so that the leftmost point agrees with that of the data. The scaling factors ($\equiv \ln\langle F_2 \rangle_{\text{data}} - \ln\langle F_2 \rangle_{\text{MC}}$) are 0.0037, 0.0161, 0.0991, and 0.0183 for (a)–(d), respectively. Note the extremely expanded vertical scale.

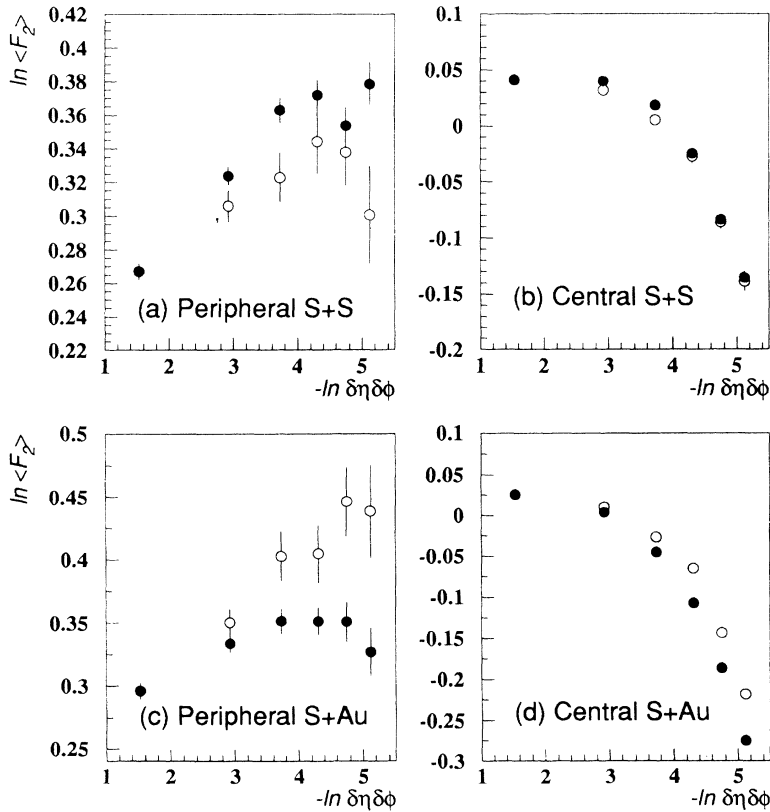


FIG. 9. $\ln\langle F_2 \rangle$ as a function of $-\ln(\delta\eta\delta\phi)$, for (a) peripheral and (b) central $^{32}\text{S}+\text{S}$ collisions, (c) peripheral and (d) central $^{32}\text{S}+\text{Au}$ collisions. Solid points: data; open points: Monte Carlo. The moments of the Monte Carlo calculation have been scaled so that the leftmost point agrees with that of the data. The scaling factors ($\equiv \ln\langle F_2 \rangle_{\text{data}} - \ln\langle F_2 \rangle_{\text{MC}}$) are 0.0273, 0.0224, 0.0956, and 0.0194 for (a)–(d), respectively.

exhibit somewhat smaller slopes and more sagging than do those of the Monte Carlo.

We conclude from the comparisons in Figs. 8 and 9 that the data do not exhibit one- or two-dimensional intermittency beyond that contained in the simulation. FRITIOF contains no intermittency for heavy-ion collisions, as has been amply demonstrated in Refs. [19,20], so that the slopes observed in the simulations are due exclusively to experimental effects such as γ conversion, resonance decays and showering in material, whose fluctuations are more apparent in the peripheral collisions than in central collisions. Our results are consistent with no intermittency from primary particle production in heavy-ion collisions. It remains to be shown that we have sensitivity to intermittency in the collision at all, and that our results are not dominated by experimental effects. This will be done in the next section.

VII. ALPHA MODEL CALCULATIONS

In order to obtain a deeper understanding of the experimental effects contributing to the observed dependence of $\langle F_q \rangle$ on $\delta\eta$ and $\delta\phi$, we have studied a more schematic simulation based on the alpha model [7,34] in two dimensions [35,36]. This is a simple, analytically solvable cascade model that generates truly intermittent distributions to arbitrarily small scale in phase space. It allows us to isolate and study experimental effects in an approximate way, independent of the complex simulation and reconstruction procedures used in the data analysis.

In the notation of [7], the alpha model slope is given by

$$\phi_q = \frac{\ln \langle W^q \rangle}{\ln \lambda}, \quad (6)$$

where W is a random function associated with each bin, $\langle \dots \rangle$ denotes mean value, and λ is the number of subdivisions of a bin in each step of the cascade. The case of

$\lambda = 2$ was studied in [7]. We have used $\lambda = 4$; that is, given an initial phase-space area $\Delta\eta\Delta\phi$, the bins of the first subdivision have area $\Delta\eta\Delta\phi/4$, those of the second subdivision $\Delta\eta\Delta\phi/16$, etc.

Particles were generated in $\eta - \phi$ space with $dN/d\eta = 48$ and 115, corresponding to the measured track densities of central $^{32}\text{S}+\text{S}$ and $^{32}\text{S}+\text{Au}$ events, respectively. Eight generations of cascade were used (this is our practical computational limit). A large phase-space interval was used for the particle generation, and the bin boundaries were shifted by a random amount in both η and ϕ to prevent artifacts due to the fixed phasing of the bins for particle generation and the bins for scaled factorial moment analysis [15]. The tracks within the WA80 acceptance were then projected onto a plane 8 m distant from their “target vertex.” The intersection of these tracks with the plane constituted a “hit” which could be altered in two ways: efficiency, 81% of the hits were kept to simulate the 90% efficiency of each detector plane and the requirement of a coincidence between them; and two-track resolution, hits lying within $dx = 2$ cm and $dy = 5$ cm of each other were merged into a single large hit to approximate the effect of finite cluster sizes (see Sec. III).

The resulting hit distributions were analyzed for one- and two-dimensional intermittency using the same method as described in Sec. IV, but with a subsample size of 1000 events.

Results from calculations with the alpha model are given in Fig. 10. Also shown are the data (solid circles) and Monte Carlo moments (open circles) for central $^{32}\text{S}+\text{S}$ and $^{32}\text{S}+\text{Au}$ events. The solid line corresponds to the intermittency slope $\phi_q = 0.029$ for “semicentral” $\text{S}+E_m$ collisions reported in the two-dimensional analysis of Ref. [17]. Using Eq. (6), alpha model parameters for the numerical calculations were chosen to reproduce slopes of $\phi_q = 0.029, 0.015$, and 0.00: the latter represents purely Poisson multiplicity fluctuations. A hit efficiency of 100% was used for the alpha model results presented in Fig. 10.

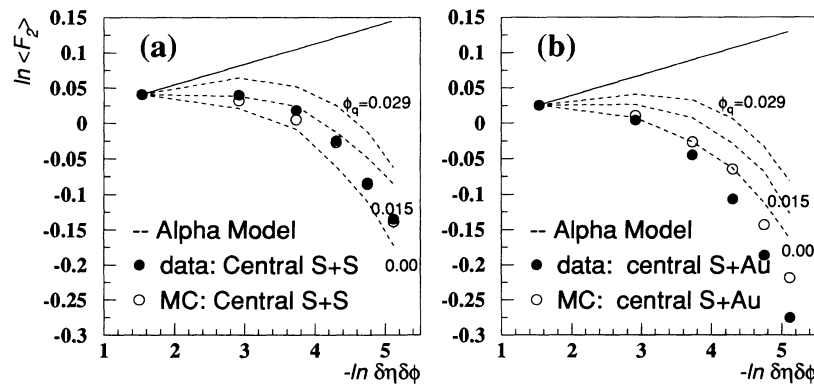


FIG. 10. $\ln \langle F_2 \rangle$ as a function of $-\ln(\delta\eta\delta\phi)$ for alpha model calculations (dashed lines) with slopes 0.029, 0.015, and 0.0: (a) $dN/d\eta = 48$: solid (open) circles are data (Monte Carlo results) for central $^{32}\text{S}+\text{S}$ events; (b) $dN/d\eta = 115$: solid (open) circles are data (Monte Carlo results) for central $^{32}\text{S}+\text{Au}$ events. In both cases the solid line represents the alpha model for a slope of 0.029 but without hit merging due to the finite two-track resolution. All alpha model calculations have been scaled vertically so that their leftmost point in the plot matches that of the data. A hit efficiency of 100% was assumed.

When imposing the two-track resolution described above, the alpha model distributions (dashed lines) in Fig. 10 sag at small resolution, in qualitative agreement with the distributions seen in the data. In contrast, it was found that neither (i) the finite number of cascade generations in the numerical calculation, nor (ii) the limited WA80 acceptance in η and ϕ , nor (iii) the efficiency of the streamer tubes individually caused a significant deviation of the resulting factorial moments from the expected power-law behavior, as exemplified by the solid line. All alpha model calculations have been scaled vertically so that their leftmost point in the plot matches that of the data. The deviation from a power-law behavior (i.e., the vertical distance between the solid line and the topmost dashed line for the case of $\phi_q = 0.029$) increases rapidly as a function of decreasing bin sizes in η and ϕ and increasing pseudorapidity density.

These results demonstrate that the two-track resolution dominates the behavior of the factorial moments at fine resolution in our experiment. Note that even though the two-track resolution is ≈ 0.03 in both η and ϕ , the sagging of the moments is noticeable at a scale an order of magnitude larger in $\delta\eta$ and $\delta\phi$ than the resolution itself. This can be understood in terms of the truncation from above of the multiplicity distribution in any bin by the merging of very close-lying tracks. The values of the factorial moments are strongly dependent upon the high-multiplicity tail, as will be demonstrated in the next section. They are strongly affected by this truncation, which becomes more probable as the bin multiplicity becomes larger, as it does for central collisions.

In spite of this drastic effect, by comparing the alpha model calculations for different slopes it is seen that we retain some sensitivity in our measurement to intermittency in these collisions. We argue that the magnitude of the difference between the alpha model curves for $\phi_q = 0.029$ and 0.0 are indicative of the magnitude of the difference that would be seen in the data for two physics scenarios of no intermittency and that seen by the KLM [17] collaboration. As can be observed, however, the data and Monte Carlo are much closer than this difference, which leads us to conclude that intermittency at the level observed by KLM is not present in our data. Because of the crude implementation of the detector re-

sponse in the alpha model, one should make quantitative comparisons of the data only to the Monte Carlo results and not the alpha model results.

VIII. EXPERIMENTAL BIASES

In this section we discuss statistical and experimental biases, in addition to two-track resolution effects, that are present in all factorial moment analyses, and which affect the estimation of the *magnitude* of the factorial moments.

A. Statistical biases

The magnitudes of scaled factorial moments, especially those of higher order, depend strongly on the number of events in a subsample. This is illustrated by our data in Fig. 11, which shows $\langle F_5 \rangle$ obtained from one-dimensional analyses of the same central $^{32}\text{S}+\text{Au}$ data set but using five different subsample sizes. For small subsample sizes the moments are underestimated by the same factor *at all resolution scales*. As the subsample size increases, the moments approach an asymptotic value. A statistical bias based on event sample size has been discussed previously [31,37] and arises from the fact that a scaled factorial moment is the ratio of two moments [see Eq. (5)]; scaled factorial moments are biased estimators and are systematically underestimated for finite event samples. We used a subsample size of 2000 events throughout our analysis, which is sufficiently large that this systematic effect is negligible, as illustrated in Fig. 11. Experiments with small event samples such as emulsion experiments usually have not taken this kind of bias into account in their analyses.

In addition to the statistical bias described above, there exists another effect called the “empty bin effect” [31,34], which should more accurately be named the “finite event number effect.” For a data set containing any number of events, there always exists a bin size (resolution) sufficiently small that only a few events from the set contribute to the calculation of the moments for a

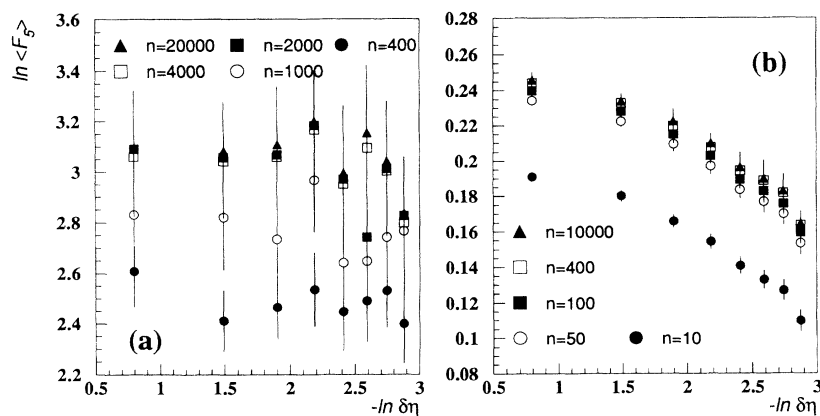


FIG. 11. $\ln\langle F_5 \rangle$ in a one-dimensional analysis, calculated for subsamples with different numbers of events, for (a) peripheral and (b) central $^{32}\text{S}+\text{Au}$ collisions.

given order q . The parent distribution of a moment calculated using only a few events is asymmetric, as shown in Fig. 5, for the higher-order moments. The most probable value of these asymmetric distributions is smaller than the mean, which results in an underestimation of the moments. All moments presented here are calculated from a sufficient number of events that their parent moment distributions are symmetric and this effect is negligible.

B. High multiplicity fluctuations

Factorial moments, especially the higher moments, are exceptionally sensitive to high multiplicity fluctuations. Figure 12 is an example of this level of sensitivity. This figure displays the peripheral $^{32}\text{S}+\text{Au}$ multiplicity distribution for tracks within the acceptance for the analysis (see Fig. 4) for approximately $\frac{1}{3}$ of the total data set. The solid line is a negative binomial (NB) fit to the data, which describes the data well except for a few high multiplicity events. One may calculate the factorial moments either from the data by using Eq. (5) or by a straightforward integration of the NB fit. If the fit is a good description of the data then the calculations should agree. Calculations for $\langle F_2 \rangle$ agree to within 1%, but $\langle F_5 \rangle$ for the NB fit calculation is a factor of 3 smaller than that obtained using Eq. (5). We have found that the disagreement is solely a consequence of the events with multiplicity ≥ 30 . Even though these events constitute only 2/10 000 of the multiplicity distribution, they practically determine the value of $\langle F_5 \rangle$.

The events at the tail of the distribution are inconsistent with the NB distribution shown in Fig. 12. The multiplicity distribution from the detector simulation does

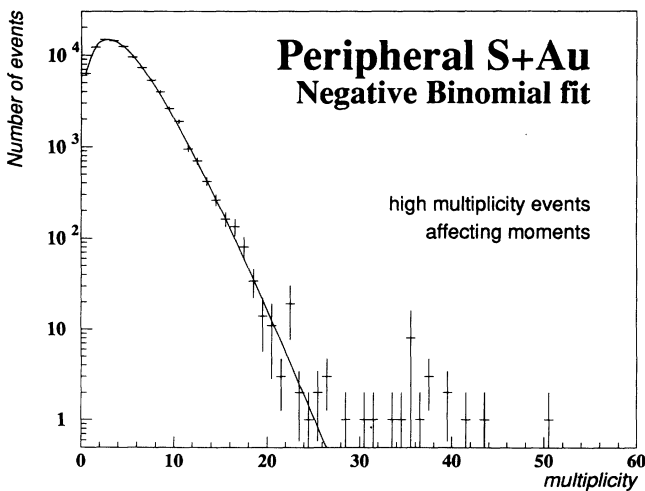


FIG. 12. Multiplicity distribution for tracks within the acceptance $\Delta\eta - \Delta\phi$ for peripheral $^{32}\text{S}+\text{Au}$ collisions. A negative binomial fit is also shown. The data for multiplicity ≥ 30 , even though they represent only 2/10 000 of the total distribution, strongly affect the value of the higher-order moments.

not exhibit such a tail. It is possible that these high multiplicity events represent another detector artifact not modeled in our detector simulation, such as streamer tube sparking, which occurs very rarely. It is also possible that they are the kind of rare physics events we are most interested in. Since it is impossible to decide this within the present analysis, we refrain from drawing conclusions based solely upon higher-order factorial moments, which are extremely sensitive to such artifacts.

IX. SCALING

We turn to the relationship between moments of different order. Two types of simple relationships or “scaling” have been discussed in the literature: scaling of the intermittency slopes [8,11]; and scaling of the moments themselves [35,38,39].

In this section we concentrate on the latter. Several scaling laws have been proposed which describe the relationship between moments of different order. Ochs [35] has pointed out that in most cascade models, if intermittency is strictly present only in a higher dimension with slope ϕ_q , then the moments calculated in a lower-dimension analysis will obey the relation

$$\ln\langle F_q \rangle = d_q + \left(\frac{\phi_q}{\phi_2} \right) \ln\langle F_2 \rangle. \quad (7)$$

If two-dimensional intermittency is present, the one-dimensional moments should “remember” the intermittency if the higher-order moments scale with $\langle F_2 \rangle$ in this fashion. Alternatively, Seibert [40] has noted that in the limit of weak fluctuations, the slopes in Eq. (7) are predicted to obey the relation $q(q-1)/2$. This result does not depend on the presence of intermittency in the factorial moments of any order but results from the mathematical nature of factorial moments.

Figure 13 is a plot of $\ln\langle F_q \rangle$ versus $\ln\langle F_2 \rangle$ for all moments in the one-dimensional analysis. The lines are fits to the data for central events (see inset window), and are extrapolated to the data for peripheral events. The slopes of the lines are 3.18 ± 0.06 , 6.80 ± 0.16 , and 12.03 ± 0.34 , for moments of order 3, 4, and 5, respectively. The predicted slopes of 3, 6, and 10 derived from the relation $q(q-1)/2$ are rather similar to the measured ones, in agreement with Ref. [40].

It is interesting that the moments exhibit this scaling in spite of the distortions induced by the two-track separation. As a test we generated the same plot as in Fig. 13 using the moments from a two-dimensional alpha model calculation (incorporating the two-track resolution) corresponding to $\phi_q = 0$, i.e., no intermittency. We observed the same scaling as seen in Fig. 13, and the slopes relating the moments of higher order to $\langle F_2 \rangle$ are similar to those quoted above. Note that the variation in the values of $\langle F_2 \rangle$ and higher moments is due, for the $\phi_q = 0$ alpha model calculation, solely to the sagging of the moments resulting from the two-track resolution. We conclude that the relationship between moments of different order expressed in Eq. (7) is probably not due to the dynamics of heavy-ion collisions [39]; for example,

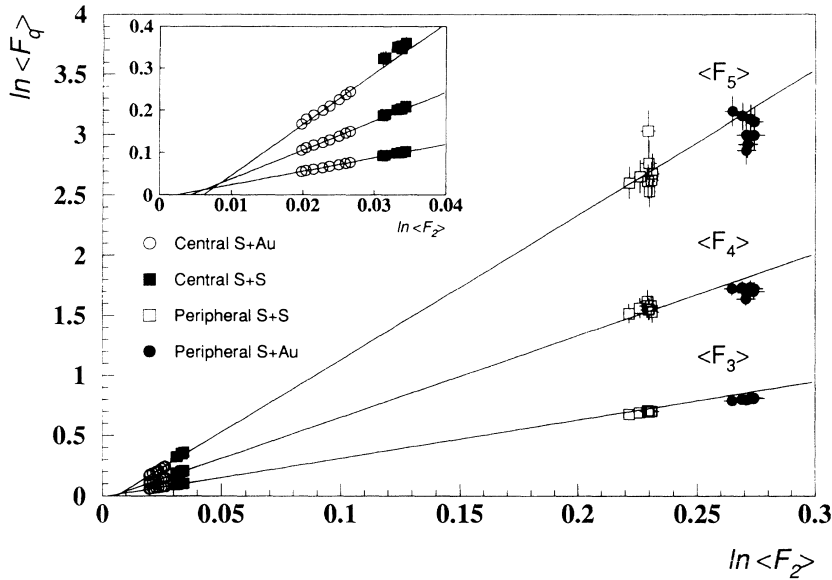


FIG. 13. $\ln\langle F_q \rangle$ vs $\ln\langle F_2 \rangle$ for all systems in the one-dimensional analysis. The inset frame expands the view for central collisions. The lines are fits to the data for central triggers extrapolated to the data for peripheral triggers.

the second moment may already contain all the relevant information of the higher moments.

X. CORRELATION FUNCTION ANALYSIS

Factorial moment analysis is extremely sensitive to a number of experimental effects, especially the two-track resolution. The WA80 Streamer Tubes have a two-track resolution of ≤ 0.03 in $d\eta - d\phi$ space; correlated particle production down to that scale should be observable with no distortions. However, the factorial moment method for investigating correlated particle production produces distortions at scales much larger than this (see discussion in Sec. VII).

An alternative method to investigate the strength and scale of correlations in particle production is to calculate the inclusive q -particle density function ρ_q [41,42], defined as

$$\rho_q(\eta_1, \dots, \eta_q) = \frac{d^q N}{d\eta_1 \dots d\eta_q} \quad (8)$$

for the joint probability per event of observing q particles with pseudorapidities (η_1, \dots, η_q) . This is the most general multiparticle quantity one can calculate; in fact, the factorial moments are calculable from the integration of ρ_q . Because of the complexity of ρ_q for $q \geq 3$, we restrict ourselves to the normalized two-particle correlation function, which is defined as

$$C(\eta_1, \eta_2) = \frac{\langle N \rangle^2}{\langle N(N-1) \rangle} \cdot \frac{\rho_2(\eta_1, \eta_2)}{\rho(\eta_1)\rho(\eta_2)}, \quad (9)$$

where N is the total multiplicity within the acceptance, $\langle \dots \rangle$ implies an average over all events, and $\rho(\eta_1)$ is simply the pseudorapidity distribution. Equation (9) can be generalized to include other variables such as ϕ_1 and ϕ_2 . We will show that the correlation function has considerable advantages over any moment analysis, and allows

one to investigate particle correlations to the scale of the detector resolution without bias.

We have performed a “traditional” two-particle correlation analysis (e.g., [43]) in $d\eta \equiv |\eta_1 - \eta_2|$ and $dR \equiv \sqrt{(\eta_1 - \eta_2)^2 + (\phi_1 - \phi_2)^2}$ [44] with the same data set as was used for the factorial moment analysis. The details of the analysis will be explained for $d\eta$ but apply to dR as well. Experimentally, the normalized two-particle correlation function can be calculated according to

$$C(d\eta) = \frac{\text{actual}(d\eta)}{\text{background}(d\eta)} \frac{N_{\text{back}}^{\text{pair}}}{N_{\text{act}}^{\text{pair}}}, \quad (10)$$

where $\text{actual}(d\eta)$ is the “actual” measured distribution of all pairs of tracks within the acceptance; $\text{background}(d\eta)$ represents the same “background” distribution of pairs within the acceptance but without correlations; and $N_{\text{act}}^{\text{pair}}$ and $N_{\text{back}}^{\text{pair}}$ are the total number of pairs in each distribution, respectively. The background distribution was constructed from artificial pairs of tracks from different events in the same data sample. To suppress residual or artificial correlations as much as possible, only events with the same multiplicity were used to generate pairs in the background distribution. The $\eta - \phi$ acceptance used to calculate $C(d\eta)$ was the same as for the scaled factorial moment analysis. No cuts or corrections were made to these distributions, as is sometimes done in intensity interferometry measurements, since we wanted to observe explicitly any distortion of $C(d\eta)$ due to the two-track resolution.

The two-dimensional correlation functions $C(dx, dy)$ and $C(d\eta, d\phi)$, defined analogously to $C(d\eta)$, were shown in Fig. 3. Figures 14 and 15 display $C(d\eta)$ and $C(dR)$ respectively for all triggers. Also shown (as grey bands) are the Monte Carlo results which were analyzed in the same fashion as the data. Since the Monte Carlo described the one-dimensional factorial moments well, the agreement between the data and Monte Carlo in Fig. 14 is not surprising, including the 1% dip at small $d\eta$ no-

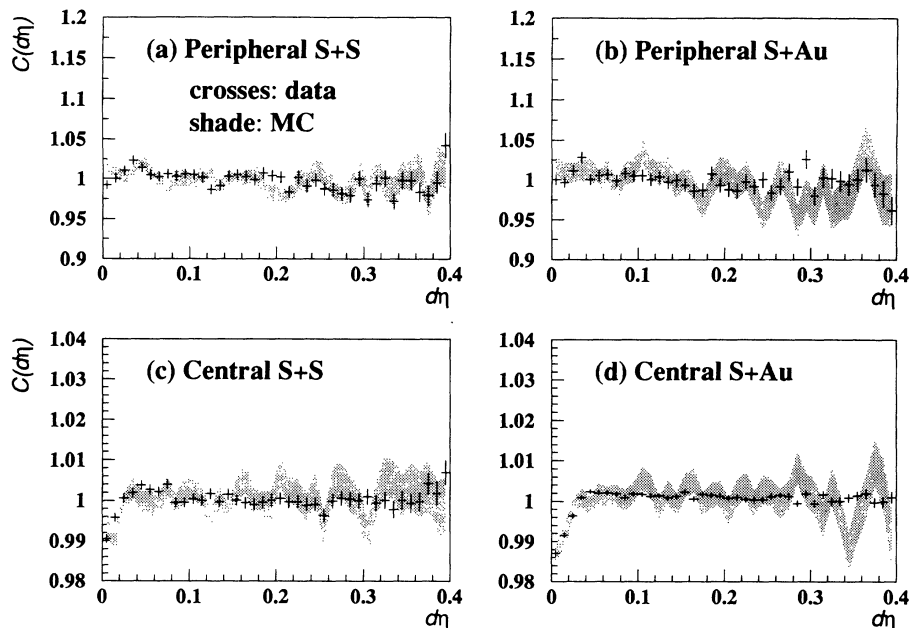


FIG. 14. Two-particle correlation function as a function of $d\eta = |\eta_1 - \eta_2|$ within the acceptance of the present analysis. The data are represented by crosses with error bars, the detector simulation by a grey band of width $\pm 1\sigma$. Note the extremely expanded vertical scale for the central trigger data.

ticeable in the central trigger data. This dip is a result of our finite two-track resolution, and is easier to observe in central events because of better statistics (note the difference in scales between the central and peripheral plots). Apart from the dip at small $d\eta$, all distributions are consistent with unity, which implies that any correlated particle production in η must occur for $d\eta < 0.05$ or $d\eta > 0.4$.

The dip in $C(d\eta)$ becomes a hole for $C(dR)$: the first few values of $C(dR)$ in all plots are outside the frame limits. Unlike $C(d\eta)$, significant correlation peaks are observed for $dR < 0.2$ in both central and peripheral collisions, though the peaks are much larger for periph-

eral collisions. The scale and strength of the correlations present in the data are reproduced reasonably well by the Monte Carlo. The peaks in these distributions are responsible for the stronger intermittency signal present in the two-dimensional factorial moments. However, because of the “hole” at small values of dR , the correlations present in central collisions were not easily observed using factorial moments.

From Figs. 14 and 15, we conclude that no correlated particle production is seen for correlation lengths $0.05 < d\eta < 0.4$ or $0.05 < dR < 1.0$ beyond that contained in FRITIOF combined with a detailed model of the detector response. This is our main physics conclusion.

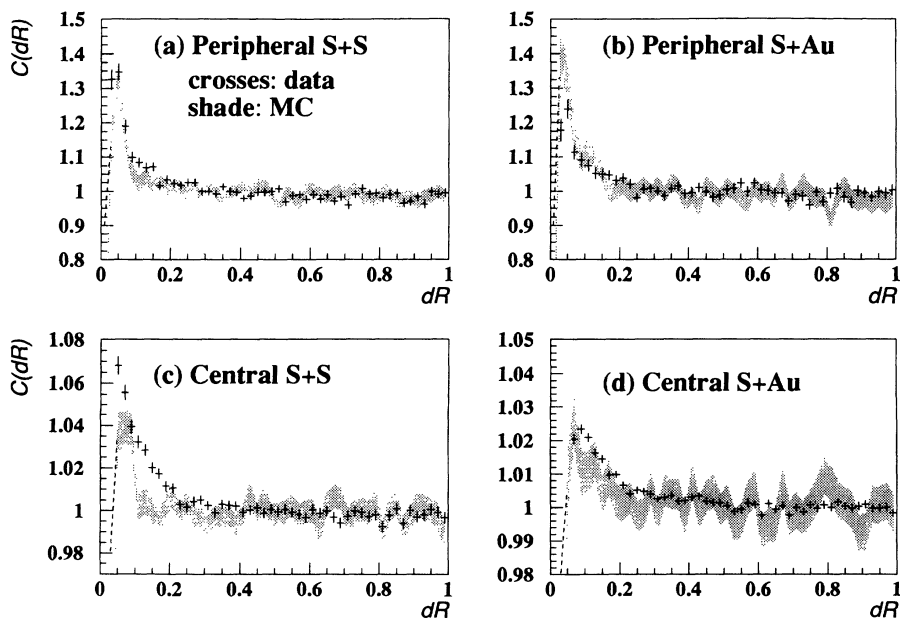


FIG. 15. Two-particle correlation function as a function of dR within the acceptance of the present analysis. The data are represented by crosses with error bars, the detector simulation by a grey band of width $\pm 1\sigma$. Note the extremely expanded vertical scale for the central trigger data.

XI. RELATIONSHIP BETWEEN THE TWO METHODS

We turn now to the relationship between the “dip” at small $d\eta$ seen in the correlation functions in Fig. 14 and the sagging seen in the factorial moments in Fig. 7. This section is motivated to a large extent by Ref. [42]. The horizontally averaged scaled factorial moments can be calculated directly from $C(d\eta)$ according to the equation

$$\langle F_2(\delta\eta) \rangle = \frac{(1/M) \sum_{m=1}^M \left(\int \int_{\Omega_m} d\eta_1 d\eta_2 \rho_2(\eta_1, \eta_2) \right)}{(\bar{N}/M)^2}, \quad (11)$$

where \bar{N} is the average multiplicity within $\Delta\eta$. The domain of integration Ω in Eq. (11) is the sum of shaded boxes Ω_m of length $\delta\eta$ on each side in Fig. 16, for factorial moments with $M = 4$ bins. The interval $\Delta\eta$ of the detector acceptance corresponds to the large box in the figure. Small values of $d\eta$ correspond to the region close to the line $\eta_1 = \eta_2$, shown as the hatched area in the figure. One expects experimental distortions of $C(\eta_1, \eta_2)$ in this region due to the two-track resolution.

If $dN/d\eta$ is constant within $\Delta\eta$, and assuming that $C(\eta_1, \eta_2) = C(d\eta)$, then it can be shown using Eq. (9) that Eq. (11) reduces to

$$\langle F_2(\delta\eta) \rangle = \frac{\langle N(N-1) \rangle}{\langle N \rangle^2} \left(\frac{1}{\delta\eta} \right)^2 \int \int_{\Omega_m} d\eta_1 d\eta_2 C(d\eta), \quad (12)$$

where Ω_m is any of the m shaded boxes. Therefore, $\langle F_2 \rangle$ is simply a two-dimensional integral of the correlation function. From inspection of Fig. 16 and applying Eq. (12), one can easily explain how the dip at small $d\eta$ is completely responsible for the sagging of the moments as follows: as M gets larger, $\delta\eta$ becomes smaller, and the domain of integration Ω becomes more tightly centered around $\eta_1 = \eta_2$. However, the “distorted” region represented by the hatched area in Fig. 16 stays the same. Hence as $\delta\eta$ gets smaller, the distorted region occupies a larger share of the domain of integration, until it completely absorbs it. Since the distortion introduced by the finite two-track separation usually decreases $C(d\eta)$, the resulting moments are smaller than they should be.

Because factorial moments represent integrals of ρ_q they use every pair of particles more than once. Thus they appear (but this is only apparent) to have better statistics than correlation functions, which use every pair only once. However, they have the serious drawback that they integrate over the region of distortion that is usually present in experiments, which in turn distorts the measured value at *all* values of $\delta\eta$, even large ones. In contrast, there is no distortion of the correlation function above some value of $d\eta$ on the order of the two-track resolution. This allows an unbiased measurement of correlations down to the two-track resolution of the detector. The interpretation of the correlation function is conceptually simpler as well: it is related to the probability that a pair of particles be produced at a fixed distance $d\eta$ in phase space. This is *not* the same as the scale $\delta\eta$ that characterizes factorial moments.

XII. CONCLUSIONS

Multiparticle production in peripheral and central collisions of $^{32}\text{S}+\text{S}$ and $^{32}\text{S}+\text{Au}$ at 200 GeV/nucleon has been studied using one- and two-dimensional scaled factorial moments in conjunction with two-particle correlation functions in η and ϕ . For all systems studied, comparisons with predictions of the FRITIOF event generator coupled with a detailed model of the WA80 detector show no observed correlated particle emission beyond that predicted by FRITIOF. This holds true for the factorial moment analysis, as well as the correlation function analysis for correlation lengths $0.05 < d\eta < 0.4$ or $0.05 < dR < 1.0$.

FRITIOF models nucleus-nucleus collisions as the convolution of multiple nucleon-nucleon collisions with no rescattering. As such it represents a model in which the resulting particle distributions are incoherent superpositions of elementary sources, without any collective behavior. Because of the agreement between the data and the simulation, we conclude that there is no evidence of collective behavior giving rise to strong intermittency in the heavy-ion collisions we have studied.

The primary experimental reason for the distortion of

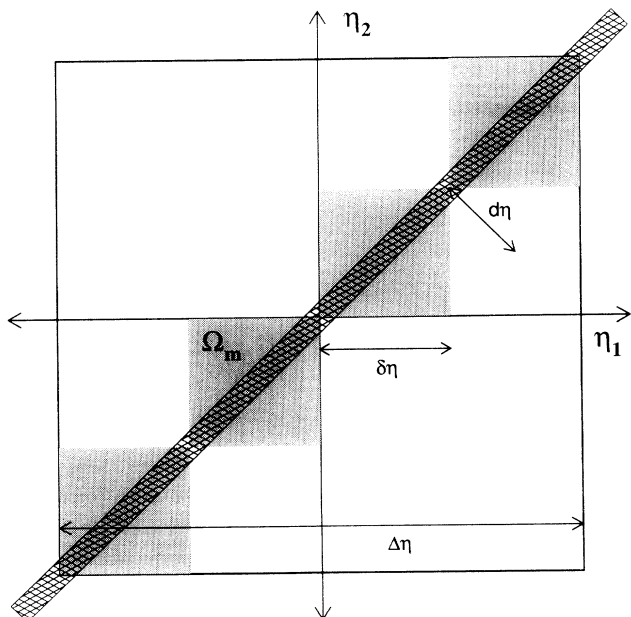


FIG. 16. Two-particle phase space (η_1, η_2) in which the two-particle density function $\rho_2(\eta_1, \eta_2)$ is defined. The large box corresponds to $\Delta\eta$ for which one-dimensional factorial moments are calculated. Shaded boxed Ω_m correspond to the bins of size $\delta\eta$ in the scaled factorial moment analysis, in this case for $M = 4$. The hatched area represents the region in which a finite two-track resolution will result in reduced efficiency.

the factorial moments for decreasing bin size has been isolated and identified as the two-track resolution of the WA80 Streamer Tube Arrays. Even though this resolution is on par with the resolution of other detectors used to study intermittency, the distortions are observed at resolution scales much larger than the two-track resolution because of the higher statistics and much larger event multiplicities as compared to previous studies. Through schematic alpha model calculations, we show that the WA80 detector is, however, sensitive to intermittency of the magnitude observed in Ref. [17]. Thus, the absence of the observation of any additional correlations in the present work beyond FRITIOF plus detector effects contradicts the conclusions of the EMU01 [19] and KLM collaborations [17].

In addition to the two-track resolution, there are additional statistical and experimental biases which render the interpretation of factorial moments in heavy-ion collisions problematical. The observation of Ochs scaling in the higher-order moments underscores this point. The connection between the scaled factorial moments and the two-particle correlation function has been investigated,

and we have shown that the correlation function isolates these effects in a simpler way, allowing clearer physics conclusions at the scale of the two-track resolution of the detector.

ACKNOWLEDGMENTS

We would like to thank the accelerator division of CERN for their excellent work. We also enjoyed many important and stimulating conversations with many people on the topic of intermittency. In particular, the authors would like to thank Scott Pratt, Erwin Friedlander, Ivo Derado, Hans Eggers, Ju Kang, Xin-Nian Wang, Wolfgang Ochs, Rudi Hwa, Peter Seyboth, Dean Chacon, Richard Morse, Andrej Białas, and Miklos Gyulassy. This work was supported jointly by the German BMFT, the Swedish Natural Science Research Council, the Humboldt Foundation, and by the Director, Office of Energy Research, Division of Nuclear Physics of the Office of High Energy and Nuclear Physics of the U.S. Department of Energy under Contract DE-AC03-76SF00098.

-
- [1] M. Bengtsson and T. Sjöstrand, *Phys. Lett. B* **185**, 435 (1987); T. Sjöstrand and M. Bengtsson, CERN Pool Programs W5035 Long Writeup, JETSET version 7.2.
- [2] G. Marchesini and B. Webber, *Nucl. Phys.* **B310**, 461 (1988).
- [3] H. Sorge, H. Stöcker, and W. Greiner, *Nucl. Phys.* **A498**, 567c (1989); C. Hartnack *et al.*, *ibid.* **A538**, 53c (1992).
- [4] K. Werner and P. Koch, *Phys. Lett.* **242**, 251 (1990); K. Werner, *Nucl. Phys.* **A544**, 593c (1992).
- [5] B. Nilsson-Almqvist and E. Stenlund, *Comput. Phys. Commun.* **43**, 387 (1987).
- [6] *Proceedings of the Santa Fe Workshop on Intermittency in High Energy Collisions*, Los Alamos, New Mexico, 1990, edited by F. Cooper, R. C. Hwa, and I. Sarcevic (World Scientific, Singapore, 1991); for a brief overview, see L. Van Hove, *Mod. Phys. Lett. A* **4**, 1867 (1989); for a theoretical overview, see R. C. Hwa, in *Quark-Gluon Plasma-Advanced Series in Directions in High Energy Physics*, edited by R. C. Hwa (World Scientific, Singapore, 1990), Vol. 6, p. 665.
- [7] A. Białas and R. Peschanski, *Nucl. Phys.* **B273**, 703 (1986).
- [8] A. Białas and R. Peschanski, *Nucl. Phys.* **B308**, 857 (1988).
- [9] G. Gustafson, Lund Report No. LU-TP 90-16, 1990; G. Gustafson, *Proceedings of the Santa Fe Workshop on Intermittency in High Energy Collisions*, Los Alamos, 1990, edited by F. Cooper, R. C. Hwa, and I. Sarcevic (World Scientific, Singapore, 1991), pp. 237–258c.
- [10] A different definition of $\langle F_q \rangle$ has been given for a fixed total multiplicity [7], along with other definitions [38]. However, Eq. (5) is appropriate for the analysis presented in this paper.
- [11] J. Wosiek, *Acta Phys. Pol. B* **19**, 863 (1988); H. Satz, *Nucl. Phys.* **B326**, 613 (1989); A. Białas and R. C. Hwa, *Phys. Lett. B* **253**, 436 (1991); J. Pan, *Phys. Rev. D* **46**, R19 (1992).
- [12] G. Gustafson and A. Nilsson, *Z. Phys. C* **52**, 533 (1991).
- [13] W. Ochs and J. Wosiek, *Phys. Lett. B* **214**, 617 (1988).
- [14] P. Abreu *et al.*, DELPHI Collaboration, *Phys. Lett. B* **247**, 137 (1990); M. Z. Akrawy *et al.*, OPAL Collaboration, *ibid.* **262**, 351 (1991); D. Decamp *et al.*, ALEPH Collaboration, *Z. Phys. C* **53**, 21 (1992).
- [15] H. J. Behrend *et al.*, CELLO Collaboration, *Phys. Lett. B* **256**, 97 (1991).
- [16] W. Braunschweig *et al.*, TASSO Collaboration, *Phys. Lett. B* **231**, 548 (1989).
- [17] R. Holynski *et al.*, KLM Collaboration, *Phys. Rev. Lett.* **62**, 733 (1989); *Phys. Rev. C* **40**, R2449 (1989).
- [18] T. Åkesson *et al.*, HELIOS-Emulsion Collaboration, *Phys. Lett. B* **252**, 303 (1990).
- [19] M. I. Adamovich *et al.*, EMU01 Collaboration, *Phys. Rev. Lett.* **65**, 412 (1990).
- [20] M. I. Adamovich *et al.*, EMU01 Collaboration, *Z. Phys. C* **49**, 395 (1991); *Phys. Lett. B* **263**, 539 (1991); *Nucl. Phys.* **B388**, 3 (1992).
- [21] J. Bächler *et al.*, NA35 Collaboration, *Z. Phys. C* **61**, 551 (1994).
- [22] R. Albrecht *et al.*, WA80 Collaboration, *Phys. Lett. B* **221**, 427 (1989).
- [23] R. Albrecht *et al.*, WA80 Collaboration, *Nucl. Phys.* **A544**, 183c (1992).
- [24] R. Albrecht *et al.*, WA80 Collaboration, Gesellschaft für Schwerionenforschung Report No. GSI-85-32, D-64220 Darmstadt, 1985.
- [25] H. Baumeister *et al.*, *Nucl. Instrum. Methods Phys. Res. Sect. A* **292**, 81 (1990).
- [26] T. C. Awes *et al.*, *Nucl. Instrum. Methods Phys. Res. Sect. A* **279**, 497 (1989); G. R. Young *et al.*, *ibid.* **279**, 503 (1989); R. Albrecht *et al.*, *Phys. Rev. C* **44**, 2736 (1991).
- [27] R. Albrecht *et al.*, *Nucl. Instrum. Methods Phys. Res.*

- Sect. A **276**, 131 (1989).
- [28] A. Eklund *et al.*, WA80 Collaboration, Nucl. Phys. **A525**, 657c (1991); R. Albrecht *et al.*, Z. Phys. C **55**, 539 (1992).
- [29] E. Iarocci, Nucl. Instrum. Methods Phys. Res. **217**, 30 (1983).
- [30] K. Fialkowski *et al.*, Acta Phys. Pol. B **20**, 639 (1989).
- [31] P. Lipa, H. C. Eggers, F. Botterweck, and M. Charlet, Z. Phys. C **54**, 115 (1992).
- [32] R. Brun *et al.*, GEANT3 *User's Guide*, CERN DD/EE/84-1.
- [33] B. Blättel *et al.*, Nucl. Phys. **A544**, 479c (1992).
- [34] P. Desvallées, R. Ouziel, and R. Peschanski, Phys. Lett. B **235**, 317 (1990).
- [35] W. Ochs, Phys. Lett. B **247**, 101 (1990); Z. Phys. C **50**, 339 (1991).
- [36] M. A. Bloomer *et al.*, WA80 Collaboration, Nucl. Phys. **A544**, 543c (1992); P. Jacobs *et al.*, WA80 Collaboration, *ibid.* **A545**, 311c (1992).
- [37] E. M. Friedlander, Mod. Phys. Lett. A **4**, 2457 (1989).
- [38] D. Seibert, Phys. Rev. D **41**, 3381 (1990).
- [39] R. C. Hwa and M. T. Nazirov, Phys. Rev. Lett. **69**, 741 (1992).
- [40] D. Seibert, Phys. Lett. B **254**, 253 (1991); J. D. de Deus, *ibid.* **278**, 377 (1992).
- [41] K. L. Wieand, S. E. Pratt, and A. B. Balantekin, Phys. Lett. B **274**, 7 (1992).
- [42] P. Lipa, P. Carruthers, H. C. Eggers, and B. Buschbeck, Phys. Lett. B **285**, 300 (1992).
- [43] T. Abbott *et al.*, E802 Collaboration, Phys. Rev. Lett. **69**, 1030 (1992).
- [44] If we define the angle between two tracks as ψ , then it can be shown for small values of ψ that $\psi \approx |\sin\theta|dR$. This approximation is quite good for the range of dR used in this analysis. Using the relation $\sin\theta = \cosh^{-1}\eta$, then $|\sin\theta|$ varies between 0.152 and 0.237 over the acceptance used in this analysis.

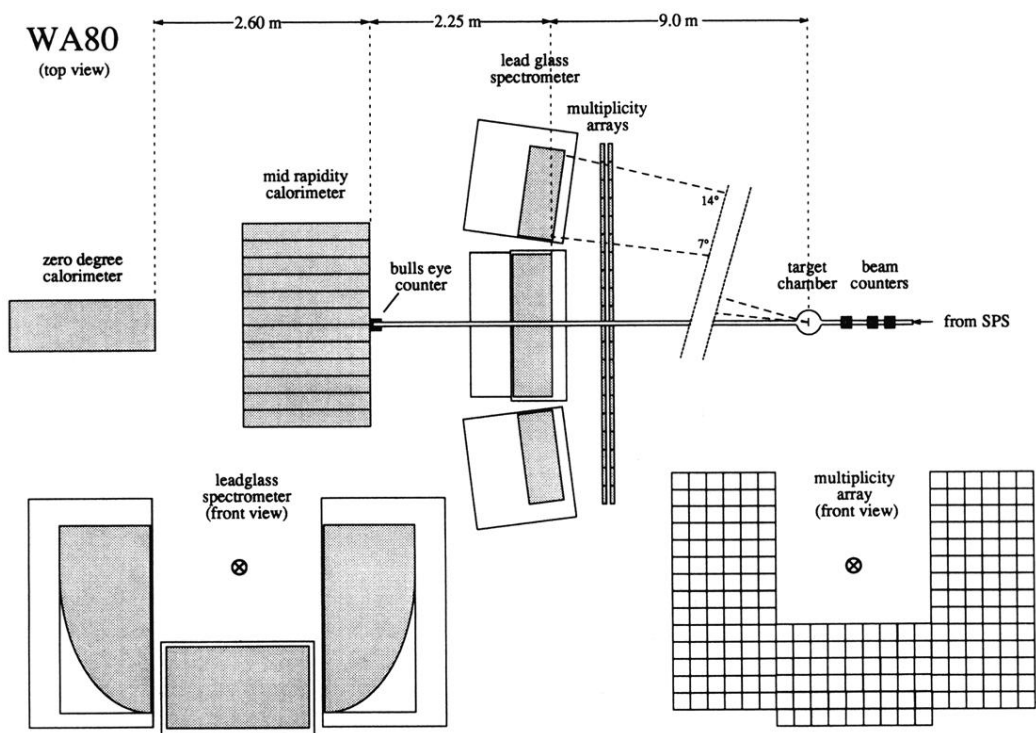


FIG. 1. 1990 WA80 experimental setup.

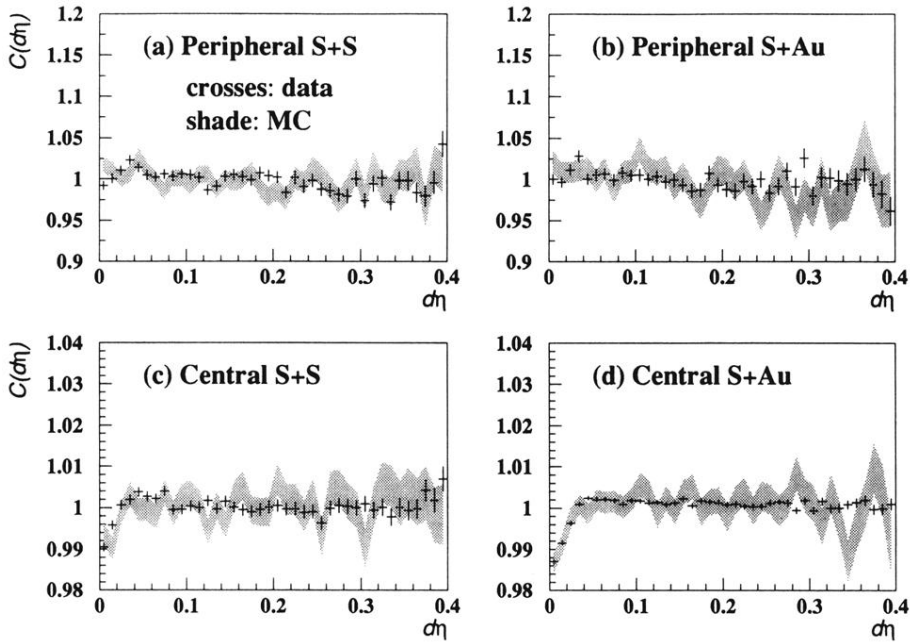


FIG. 14. Two-particle correlation function as a function of $d\eta = |\eta_1 - \eta_2|$ within the acceptance of the present analysis. The data are represented by crosses with error bars, the detector simulation by a grey band of width $\pm 1\sigma$. Note the extremely expanded vertical scale for the central trigger data.

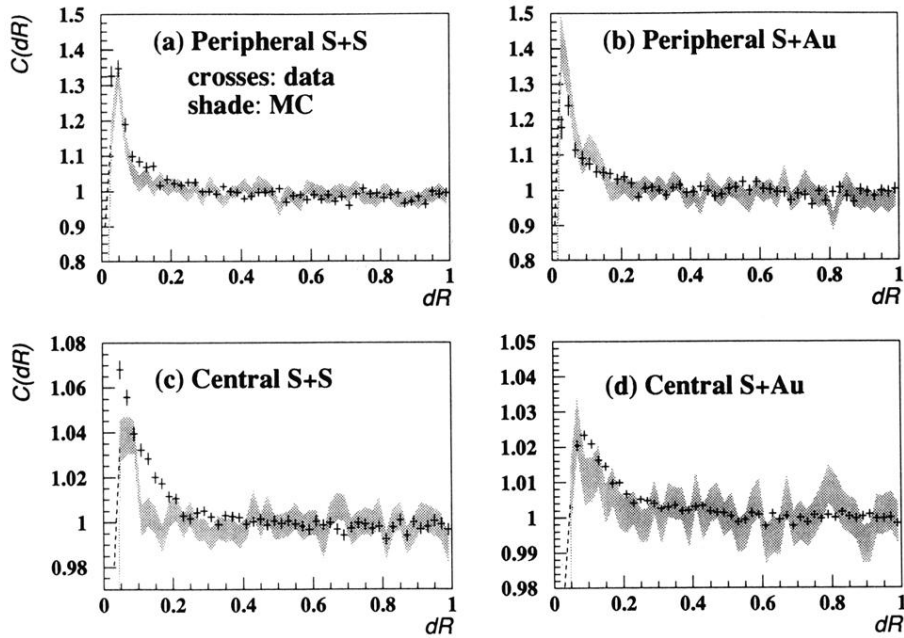


FIG. 15. Two-particle correlation function as a function of dR within the acceptance of the present analysis. The data are represented by crosses with error bars, the detector simulation by a grey band of width $\pm 1\sigma$. Note the extremely expanded vertical scale for the central trigger data.

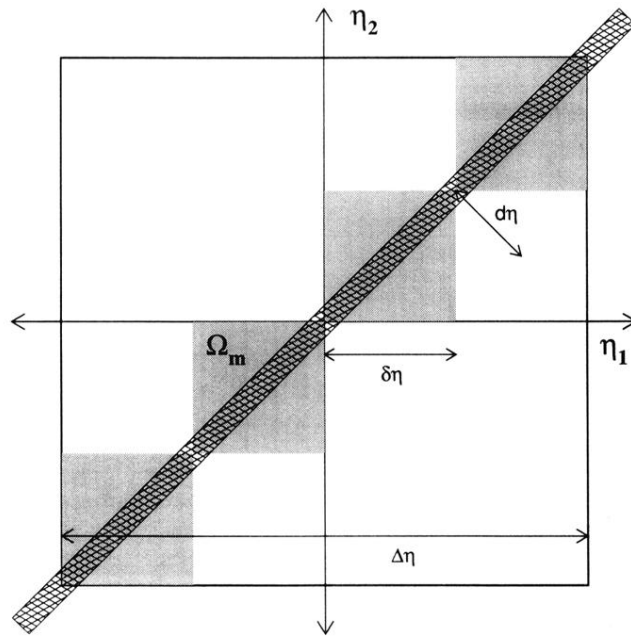


FIG. 16. Two-particle phase space (η_1, η_2) in which the two-particle density function $\rho_2(\eta_1, \eta_2)$ is defined. The large box corresponds to $\Delta\eta$ for which one-dimensional factorial moments are calculated. Shaded boxed Ω_m correspond to the bins of size $\delta\eta$ in the scaled factorial moment analysis, in this case for $M = 4$. The hatched area represents the region in which a finite two-track resolution will result in reduced efficiency.

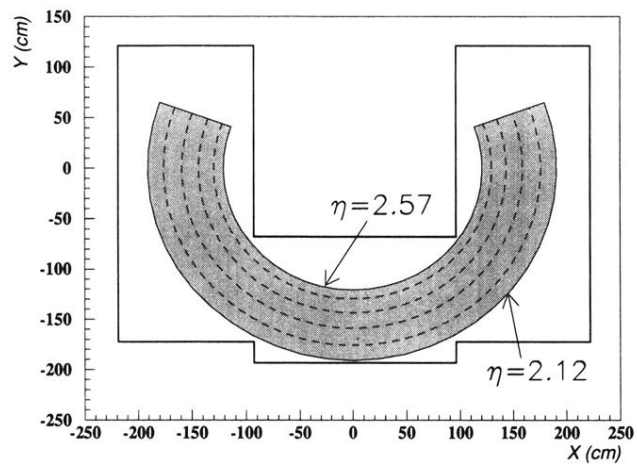


FIG. 4. Phase-space acceptance for scaled factorial moment analysis ($\Delta\eta = 0.45$, $\Delta\phi = 220^\circ$). Solid line indicates outline of actual streamer tube detector.

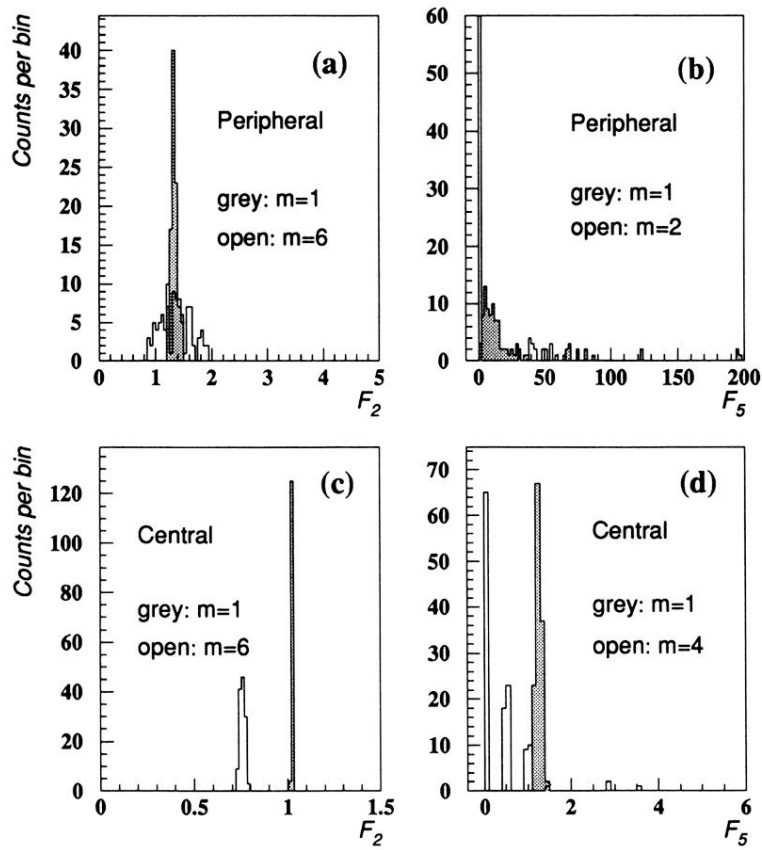


FIG. 5. Subsample distributions of $\langle F_q \rangle$ for a two-dimensional analysis of $^{32}\text{S}+\text{Au}$ collisions. Each frame shows the distributions of the same moment for different bin sizes. Peripheral events: (a) $\langle F_2 \rangle$ and (b) $\langle F_5 \rangle$. Central events: (c) $\langle F_2 \rangle$ and (d) $\langle F_5 \rangle$.